

Scalability of Graph Neural Network in Accurate Prediction of Force Chain Network in Suspensions

Armin Aminimajd,¹ Joao Maia,¹ and Abhinendra Singh^{1,*}

¹*Department of Macromolecular Science and Engineering,
Case Western Reserve University, Cleveland, OH, 10040, USA*

(Dated: September 23, 2024)

Dense suspensions often exhibit shear thickening, characterized by a dramatic increase in viscosity under large external forcing. This behavior has recently been linked to the formation of a system-spanning force chain network (FCN), which contributes to increased resistance during deformation. However, identifying these force chains poses experimental challenges and is computationally expensive. This study introduces a Graph Neural Network (GNN) model designed to accurately predict FCNs in two dimensional simulations of dense shear thickening suspensions. The results demonstrate the GNN model's robustness and scalability across various stress levels (σ), packing fractions (ϕ), system sizes, particle size ratios (Δ), and amount of smaller particles. The model is further able to predict both the occurrence and structure of the FCN. The presented model is accurate and interpolates and extrapolates to conditions far from its control parameters. This machine learning approach provides more accurate, cheaper, and faster predictions of suspension properties as compared to conventional methods, while using only small systems. Ultimately, our findings pave the way for predicting force chain networks in real-life large-scale polydisperse suspensions, for which theoretical models are largely limited due to computational challenges.

Introduction: Dense particulate suspensions are ubiquitous in natural, human health, and industrial settings, with examples ranging from mud to blood, to paint and cement [1–4]. Under external deformation, they exhibit diverse non-Newtonian complex rheological behaviors, such as yielding, normal stress differences, shear-thinning, shear thickening, or even jamming [5–8]. Shear thickening (ST) is a non-linear phenomenon where the viscosity η increases continuously (CST) or discontinuously (DST) with increasing shear rate $\dot{\gamma}$ at a given volume fraction ϕ [9]. A vast body of research has linked the non-Newtonian rheology in dense suspensions to constraints on the relative motion that stabilizes the force and contact network under applied deformation [5, 10–15]. As such, many recent studies have used network science techniques to characterize and analyze the properties of these networks [14–20] and correlating them with the resultant rheology. For instance, in dry granular materials, the mesoscale network features have been linked to the emergence of rigidity [21], sound propagation [22], and non-locality [23] in case of both frictionless and frictional particle packings. Therefore, accurately and easily identifying the force networks in amorphous materials, specifically in flowing dense suspensions, is highly beneficial for understanding and developing the statistical physics framework for rheological response.

However, identifying FCN in most particulate suspensions remains challenging due to the limitations of experimental methods and the complex nature of particulate systems. State-of-art experimental efforts are limited by the protocol to freeze the sheared microstructure, along with the cost and toxicity of chemicals used to generate model suspension system [13, 24, 25]. These force chains are rather readily accessible in discrete particle simula-

tions; however, traditional methods remain computationally expensive, making large system sizes computationally intractable even with the recent advances in computational power. The two fundamental questions that still remain unanswered: (i) How can the force chains under applied stress be predicted, *i.e.*, is it possible to predict which particles will be in contact? (ii) Next, can the structure of the force chain network for various solid concentrations, system size, particle size dispersity, and applied stresses be predicted?

Recently, a more promising avenue has been the use of Machine Learning techniques [26–31]. Among diverse ML techniques, Graph Neural Networks (GNN) have exhibited superior performance compared to traditional methods, mainly owing to their more expressive and adeptness in handling unstructured data, making them an ideal candidate for predicting the force chain network. Most work in particulate suspension has focussed only on the dilute limit [28–30], not extrapolatable to the dense limit, of interest here. In the dense limit, Mandal et al. [26] employed GNN in dry granular matter, demonstrating FCN prediction in both frictionless and frictional materials from the undeformed structure. Although novel, the simulations were performed for relatively high volume fractions close to or above jamming, which is not feasible for rigid particles, and the work lacked extrapolation capability.

This letter addresses previously mentioned challenges of predicting the structure of FCN in dense suspensions only with the knowledge of the relative distance between particles by employing a robust GNN approach to a well-established simulation approach for dense suspensions [10, 11, 32–36]. By comparing the predictions from the ML technique with simulation results, it is demon-

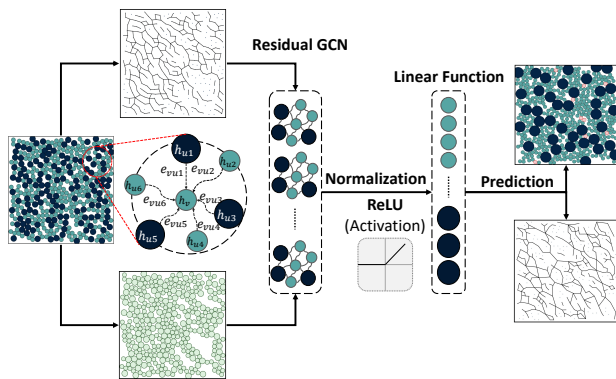


FIG. 1. **Schematic of the Graph Neural Network (GNN) for predicting FCN.** Initially, the simulation configuration is transformed into a graph comprising its constituent particles and the force chain network. These particles and the chain network, analogous to nodes and edges in the graph, undergo processing through residual convolutional layers. The message-passing process is done in these layers, employing an aggregation function to update information across nodes and edges. Subsequently, a non-linear activation function (ReLU) is applied to enhance the model’s prediction capabilities, particularly in capturing complex relationships. A linear function is applied to assign each node to a specific class for classification. To mitigate overfitting, regularization techniques such as dropout are employed at the final stage of the model.

stated that the GNN model can accurately predict not only the force chains, i.e., the particles that will be in contact, under applied stress, but also the structure factor of the FCN. In addition, the mentioned capabilities hold for many values of volume fraction ϕ and applied stress σ even when the machine has not seen those conditions. Finally, this work can help make meaningful predictions about suspension properties for computationally and experimentally challenging cases (large system sizes, truly polydisperse particles, etc.) while being trained on less challenging conditions within reasonable computational cost & time.

Simulating dense suspensions: Though the real-world dense suspensions are three-dimensional, related prior works have shown flow behavior for 2D and 3D to be similar if the volume fraction ϕ is appropriately scaled [17, 18]. Thus, two-dimensional simulations (a monolayer of spheres) are performed for clarity, simplicity, computational efficiency, and as a first demonstration of application of GNN to predict the FCN. The simulation scheme (LF-DEM) integrates two modeling approaches: Lubrication flow (LF) and the discrete element DEM method from dry granular materials [5, 10, 11, 37]. The contact forces include both normal and tangential frictional forces. The particle motion is considered to be inertialess, i.e., particles obey the overdamped equation of motion $\mathbf{F}_C + \mathbf{F}_H = 0$, where $\mathbf{F}_C = \mathbf{F}_C^N + \mathbf{F}_C^T$. Here, \mathbf{F}_H , \mathbf{F}_C^N , and \mathbf{F}_C^T denote the hydrodynamic lu-

brication, contact normal, and contact tangential forces with $|\mathbf{F}_C^T| \leq \mu |\mathbf{F}_C^N|$ ($\mu = 0.5$ is the friction coefficient). The Critical Load Model (CLM) introduces rate dependence, where the normal force $F_C^N \geq F_0$ is needed to activate interparticle friction, giving a characteristic stress scale $\sigma_0 = F_0/a^2$. A series of stress-controlled simple shear flows are simulated for $N = 400$ to 5000 non-Brownian bidisperse particles with Lees-Edwards periodic boundary condition in a unit cell with particle size ratio $\Delta = R_L/R_S$ and different volumetric mixing ratios $\alpha = V_S/(V_L + V_S)$. Here, R_S (R_L) and V_S (V_L) are the radii and volume of small (and large) particles, respectively. This work focuses on the frictional force network, which is the primary driver for DST [10, 11, 37, 38].

Machine learning methodology: The concept is adapted from Li *et al.*, which made very deep training of graphs based on graph convolutional neural network (GCN) possible by incorporating residual and dense connections, along with the use of dilated convolutions to remedy vanishing gradient problem [39, 40]. Their technique called deep graph convolutional neural network (DeepGCN) is used, and then the models are optimized by training them at different hyperparameters. Compared to the traditional GCN, this deep learning method provides more reliable and deeper training and an interpretable representation of large graphs and node property prediction tasks in dense particulate systems [39]. This node classification approach identifies particles in frictional contact and participate in FCN.

Figure 1 presents the process and architecture of our DeepGCN. To train the model, first, the dynamic simulation dataset is transformed into graphs by treating particles as nodes and drawing edges (e_{ij}) between them to represent their interactions. The node features include particle radius and other global simulation details, like packing fraction ϕ , applied shear stress σ/σ_0 , etc. The edges representing interactions called edge attributes contain information about the distance between particles (r_{ij}), x and y components of vector r_{ij} , Sine and Cosine of the angle r_{ij} makes with the x -axis (flow direction). The DeepGCN model consists of N_l layers, incorporating residual connections. A node’s feature vector is updated in each residual layer through a message-passing process, aggregating information from its neighbors, including nodes and connected edges within the graph. A nonlinear activation function, Relu, followed by a linear classification function is applied to the output to predict the probability pt for each particle to be a part of the FCN. More details regarding the mechanism and architecture of DeepGCN are provided in the Supplemental document.

Results: The following describes two striking features of the DeepGCN scheme for predicting force chains: robustness and scalability.

Robustness: First, the DeepGCN method is shown to be highly robust in predicting the force chains in a dy-

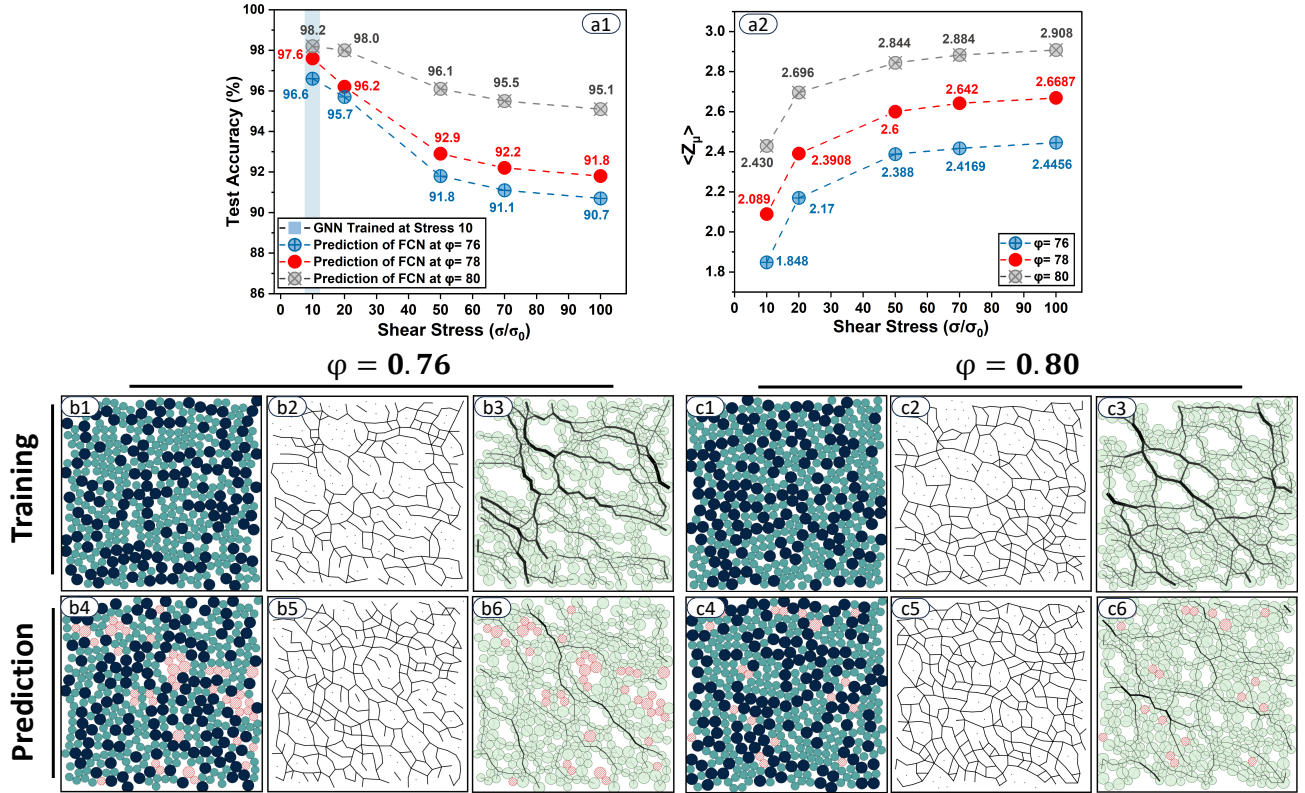


FIG. 2. **Robustness in prediction of FCN for a prototypical shear thickening suspension.** The GNN model is trained on the simulation data set at a fixed stress $\sigma/\sigma_0 = 10$ and at different packing fractions ϕ for $N = 400$ and bidispersity ($\Delta, \alpha = 1.4, 0.5$). (a1) Prediction accuracy for FCN for different values of $\phi, \sigma/\sigma_0$, with the GNN conditioned at $\sigma/\sigma_0 = 10$ for each ϕ . (a2) Frictional coordination number $\langle Z_\mu \rangle$ as a function of stress for various values of ϕ . (b1-b3) Visual of the training condition with $\phi = 0.76$, showing (b1) sheared packing, (b2) black lines showing the force chain network (FCN), and (b3) particles participating in the FCN along with the black lines showing the network. (b4-b6) Predicted configuration at $\sigma/\sigma_0 = 100$ with (b4) particle positions, (b5) FCN, and (b6) particles in contact and the FCN. Misidentified particles are shown in red. (c1-c3) Same as (b1-b3) but for $\phi = 0.8$ and $\sigma/\sigma_0 = 10$. (c4-c6) Predicted network based on (c1-c3).

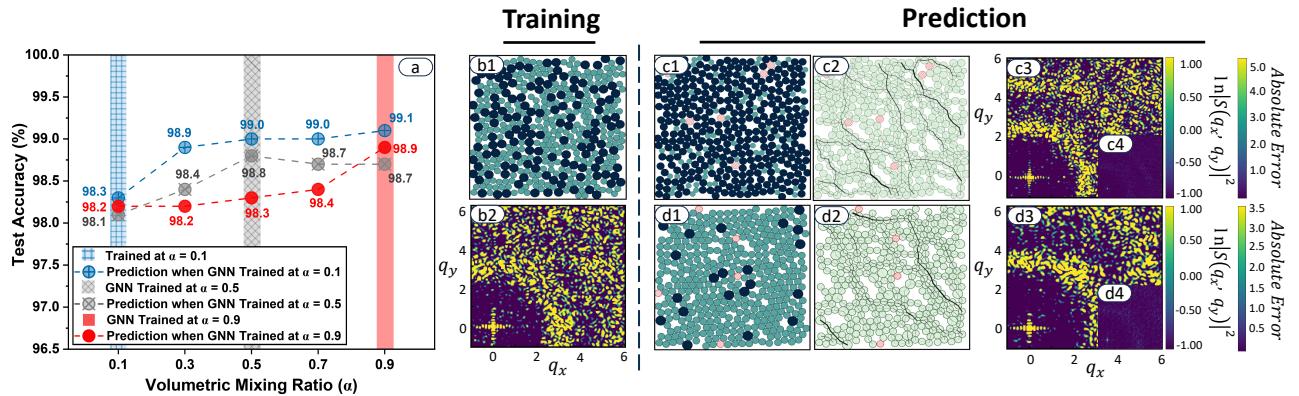


FIG. 3. **Robustness in FCN predictions for various volumetric mixing ratios α .** All the configurations are generated for $\phi = 0.76$, $\Delta = 1.4$, and sheared at fixed stress of $\sigma/\sigma = 50$. The GNN model is trained with the configuration consisting of 400 particles at different $\alpha = 0.1, 0.5$, and 0.9 and can also robustly predict the force chain network for other values of α . (b1-b2) The configuration on which the training is conditioned with (b1) showing sheared packing with dark (and light) blue showing larger (and smaller) particles, and (b2) showing the corresponding structure factor of the network. (c1-c4) The predictions for $\alpha = 0.1$: (c1) showing the configuration with all particles, (c2) only particles in contact or part of FCN with the network represented as black lines, (c3) predicted structure factor, (c4) absolute error in structure factor as compared to the simulated force chains. (d1-d4) Same as c1-c4 but for the configuration with $\alpha = 0.9$.

namical system, where the network is continuously forming and breaking due to the bulk shearing motion (Figure 2). $N = 400$ particles are used at packing fractions $\phi = 0.76, 0.78, 0.8$ with $\Delta = 1.4$ and $\alpha = 0.5$. The full rheological flowcurves ($\eta_r(\phi, \sigma/\sigma_0)$) and the frictional coordination number ($Z_\mu(\phi, \sigma/\sigma_0)$) are presented in the Supplemental Material. The suspension undergoes CST for $\phi = 0.76, 0.78$ and DST into a nearly jammed state for $\phi = 0.8$. Here, the model is trained at $\sigma/\sigma_0 = 10$ for each ϕ , and predictions are made for other applied stresses. Remarkably, despite the sensitivity of the FCN to both the stress and volume fractions, the model is capable of accurate predictions ($> 90\%$) for all values of $(\sigma/\sigma_0, \phi)$ (Fig. 2 a1). In Figs. 2 b4-b6 and c4-c6, the predictions with numerical simulation results at $\sigma/\sigma_0 = 100$ are visualized (Figs. 2 b1-b3 and c1-c3) for the corresponding $\phi = 0.76$ and 0.8 , respectively. As can be seen, only a few particles (those highlighted in red) evade the predictions of the model. Especially for $\phi = 0.8$, the training stress ($\sigma/\sigma_0 = 10$) is in an unjammed flowing state, while the prediction stress ($\sigma/\sigma_0 = 100$) is nearly in the shear-jammed state, yet an accuracy of 95% is achieved, highlighting the strength of the model. Figure 2 a2 shows Z_μ for the values of σ/σ_0 and ϕ of interest here (results for all stress values in Figs. S1 and S2 of SI). The FCN becomes increasingly interconnected, spanning both compressive and tensile directions with increasing stress. The decrease in prediction accuracy at higher stresses suggests the difficulty in predicting FCN, highlighting the increase in complexity at higher stresses. In SI, the results for training at different stresses are presented, with an enhancement in accuracy when the model is trained at higher stresses. This is expected since the model has “seen” the complex structure; hence, it can accurately predict the complex features. The results of these rigorous checks demonstrate that the model maintains a highly accurate performance, with extrapolated predictions for unseen conditions, without prior knowledge of interparticle forces and with only information on physical positions solely at a fixed stress value.

Experimental and simulation literature has shown that bidispersity drastically affects the rheology of dense particulate systems [41–45]. Hence, it is tempting to ask if the presented GNN model can predict a force chain network for different values of α . Figure 3a demonstrates the robustness of the GNN model in predicting FCN at various values of α for a fixed size ratio $\Delta = 1.4$ with the accuracy exceeding 98%. Figure 3b1 shows the training set with particle positions, with Fig. 3b2 showing the corresponding structure factor. Figures 3, c1 & d1 show the model predictions for $\alpha = 0.1$ & 0.9 (on previously unseen configurations) with remarkable predictions of the FCN (Fig. 3 c2,d2). Furthermore, the structure factor of the predicted force chain network is analyzed, as shown in Figs. 3 c3 & d3 for $\alpha = 0.1$ & 0.9 , respectively, with Figs. 3 c4 & d4 showing the absolute error of the struc-

ture factor w.r.t. the structure factor of the exact force chains. This consistent accuracy is achieved (Fig. 3 a) for all values of α even though the force network has a distinct structure (being dominated by small or large particles for the two values of α). The accuracy is *robust* to the choice of training value of α ($(0.1, 0.5, \text{ or } 0.9)$). This implies that with only having information from a limited number of particles of mostly one type, the GNN can predict the FCN for a distinct system.

Scalability: Next, the scalability of the ML model to make predictions for larger system sizes and complexities like different particle size ratios is demonstrated. This ability of the model is tested by training the model on a rather small system size ($N = 400$) at $\sigma/\sigma_0 = 50$ and $\phi = 0.76$ and then testing the predictions with not only a larger N but also a larger size ratio Δ . Figure 4 demonstrates the scalability, showing no substantial decrease in accuracy even at 10 times the system size across very different particle size ratios (from 1.4 to 6). Interestingly, larger particles are less prone to errors as they can make more contacts than smaller particles, given a larger surface area. The results show that the model can capture the relationship between particles and adapt it to large-scale systems, given only local neighborhood information.

Conclusions. This study has demonstrated the application of DeepGNN in predicting the force chain network structure in dense suspensions, utilizing fixed configurations under simple shear. The obtained DeepGNN model exhibits remarkable generalization capabilities, accurately predicting FCNs across a wide range of unseen configurations, even under conditions significantly different from its original training environment. This highlights its *scalability* and *robustness* in predicting the FCN across varying system sizes N , bidispersity (in terms of Δ and α), and applied stress σ . This DeepGNN model offers valuable insights into particle information and the force chain structure of suspensions, all without the need for explicit knowledge of interparticle interactions. This outcome underscores the scalability and robustness of the model, demonstrating its ability to generalize remarkably well to predict various systems solely based on the positions and contact information of the particles. This model is particularly appealing due to the challenges of experimentally extracting force chain networks and the computational expense of tracking system dynamics with many-body interactions and boundary conditions. Its versatility suggests potential for predicting various physical and rheological properties in three-dimensional systems. Although the current study focused only on frictional interactions, the model can be extended to incorporate attractive, repulsive, and hydrodynamic interactions, with promising applications in colloidal gels where network physics is critical to elasticity [25]. This capability will enable the exploration of large-scale, real-life systems in natural and industrial contexts, with reduced computational costs and resources.

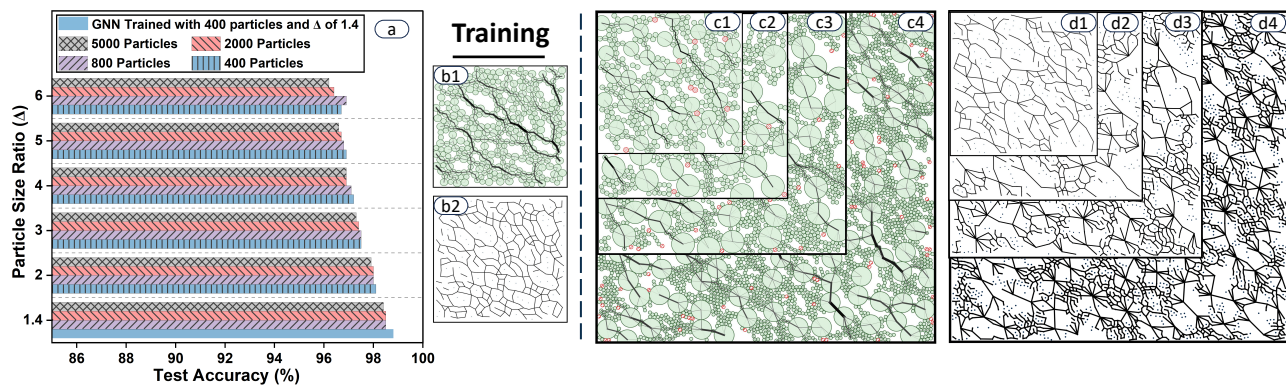


FIG. 4. **Scalability in predicting FCN across different system sizes and varying particle size ratio.** All configurations sheared at a constant scaled stress $\sigma/\sigma_0 = 50$, and packing fraction $\phi = 0.76$ and volumetric mixing ratio $\alpha = 0.5$. The model is trained on configurations with $N = 400$ for $\Delta = 1.4$. (b1-b2) represents the chain network and the particles in contact with the configuration on which the training is conditioned. (c1-c4) the prediction of chain networks at different systems, with (c1) $\{N, \Delta\} = \{400, 4\}$, (c2) $\{N, \Delta\} = \{800, 5\}$, (c3) $\{N, \Delta\} = \{2000, 6\}$, and (c4) $\{N, \Delta\} = \{5000, 6\}$. (d1-d4) Displaying the corresponding chain network for c1-c4.

Acknowledgements: All of this work made use of the High-Performance Computing Resource in the Core Facility for Advanced Research Computing at Case Western Reserve University. A. S. acknowledges Case Western Reserve University for start-up funding. S. Rogers, M. Ramaswamy, V. Sharma, and S. Pradeep are acknowledged for fruitful discussions.

* abhinendra.singh@case.edu

- [1] P. Coussot, *Mudflow Rheology and Dynamics* (CRC Press, 1997).
- [2] D. J. Jerolmack and K. E. Daniels, *Nature Reviews Physics* **1**, 716 (2019).
- [3] G. P. Galdi, R. Rannacher, A. M. Robertson, and S. Turek, *Delhi Book Store*, 8 (2008).
- [4] J. Benbow and J. Bridgewater, *Paste flow and extrusion* (Oxford University Press(UK), 1993).
- [5] J. F. Morris, *Annual Review of Fluid Mechanics* **52**, 121 (2020).
- [6] C. Ness, R. Seto, and R. Mari, *Annual Review of Condensed Matter Physics* **13**, 97 (2022).
- [7] A. Singh, *MRS Communications*, 1 (2023).
- [8] Y. C. Saraswat, E. Kerstein, and L. C. Hsiao, *Journal of Rheology* **68**, 205 (2024).
- [9] J. Mewis and N. J. Wagner, *Colloidal Suspension Rheology* (Cambridge University Press, 2011).
- [10] A. Singh, C. Ness, R. Seto, J. J. de Pablo, and H. M. Jaeger, *Physical Review Letters* **124**, 248005 (2020).
- [11] R. Mari, R. Seto, J. F. Morris, and M. M. Denn, *Journal of Rheology* **58**, 1693 (2014).
- [12] A. Boromand, S. Jamali, B. Grove, and J. M. Maia, *Journal of Rheology* **62**, 905 (2018).
- [13] S. Pradeep, M. Nabizadeh, A. R. Jacob, S. Jamali, and L. C. Hsiao, *Physical Review Letters* **127**, 158002 (2021).
- [14] O. Sedes, H. A. Makse, B. Chakraborty, and J. F. Morris, *Physical Review Fluids* **7**, 024304 (2022).
- [15] M. van der Naald, A. Singh, T. T. Eid, K. Tang, J. J. de Pablo, and H. M. Jaeger, *Nature Physics*, 1 (2024).
- [16] J. E. Thomas, K. Ramola, A. Singh, R. Mari, J. F. Morris, and B. Chakraborty, *Phys. Rev. Lett.* **121**, 128002 (2018).
- [17] M. Gameiro, A. Singh, L. Kondic, K. Mischaikow, and J. F. Morris, *Physical Review Fluids* **5**, 034307 (2020).
- [18] M. Nabizadeh, A. Singh, and S. Jamali, *Physical Review Letters* **129**, 068001 (2022).
- [19] L. E. Edens, S. Pednekar, J. F. Morris, G. K. Schenter, A. E. Clark, and J. Chun, *Physical Review E* **99**, 012607 (2019).
- [20] L. E. Edens, E. G. Alvarado, A. Singh, J. F. Morris, G. K. Schenter, J. Chun, and A. E. Clark, *Soft Matter* **17**, 7476 (2021).
- [21] S. Henkes, D. A. Quint, Y. Fily, and J. M. Schwarz, *Phys. Rev. Lett.* **116**, 028301 (2016).
- [22] E. T. Owens and K. E. Daniels, *Europhysics Letters* **94**, 54005 (2011).
- [23] A. Thomas, Z. Tang, K. E. Daniels, and N. Vriend, *Soft Matter* **15**, 8532 (2019).
- [24] S. Pradeep and L. C. Hsiao, *Soft Matter* **16**, 4980 (2020).
- [25] M. Nabizadeh, F. Nasirian, X. Li, Y. Saraswat, R. Waheibi, L. C. Hsiao, D. Bi, B. Ravandi, and S. Jamali, *Proceedings of the National Academy of Sciences* **121**, e2316394121 (2024).
- [26] R. Mandal, C. Casert, and P. Sollich, *Nature Communications* **13**, 1 (2022).
- [27] Z. Li, X. Li, H. Zhang, D. Huang, and L. Zhang, *The Journal of Chemical Physics* (2023).
- [28] N. R. Ashwin, Z. Cao, N. Muralidhar, D. Tafti, and A. Karpatne, *Powder Technology* **401**, 117303 (2022).
- [29] A. Rossi, F. Alberini, and E. Brunazzi, *Chemical Engineering Research and Design* **177**, 273 (2022).
- [30] P. Binel, A. Jain, A. Jaeggi, D. Biri, A. K. Rajagopalan, A. J. DeMello, and M. Mazzotti, *Small Methods* **7**, 2201018 (2023).
- [31] K. Galloway, E. Teich, X. Ma, C. Kammer, I. Graham, N. Keim, C. Reina, D. Jerolmack, A. Yodh, and P. Arratia, *Nature Physics* **18**, 565 (2022).

- [32] R. Mari, R. Seto, J. F. Morris, and M. M. Denn, *Physical Review E* **91**, 052302 (2015).
- [33] R. Mari, R. Seto, J. F. Morris, and M. M. Denn, *Proc. Natl. Acad. Sci. U.S.A.* **112**, 15326 (2015).
- [34] A. Singh, R. Mari, M. M. Denn, and J. F. Morris, *Journal of Rheology* **62**, 457 (2018).
- [35] A. Singh, S. Pednekar, J. Chun, M. M. Denn, and J. F. Morris, *Physical Review Letters* **122**, 098004 (2019).
- [36] A. Singh, G. L. Jackson, M. van der Naald, J. J. de Pablo, and H. M. Jaeger, *Physical Review Fluids* **7**, 054302 (2022).
- [37] R. Seto, R. Botet, M. Meireles, G. K. Auernhammer, and B. Cabane, *J. Rheol.* **57**, 1347 (2013).
- [38] C. Ness and J. Sun, *Soft Matter* **12**, 914 (2016).
- [39] G. Li, C. Xiong, A. K. Thabet, and B. Ghanem, *CoRR abs/2006.07739* (2020).
- [40] G. Li, M. Muller, A. Thabet, and B. Ghanem, in *Proceedings of the IEEE/CVF international conference on computer vision* (2019) pp. 9267–9276.
- [41] B. J. Maranzano and N. J. Wagner, *Journal of Chemical Physics* **114**, 10514 (2001).
- [42] S. Pednekar, J. Chun, and J. F. Morris, *Journal of Rheology* **62**, 513 (2018).
- [43] J. C. Petit, N. Kumar, S. Luding, and M. Sperl, *Physical Review Letters* **125**, 215501 (2020).
- [44] B. M. Guy, C. Ness, M. Hermes, L. J. Sawiak, J. Sun, and W. C. Poon, *Soft Matter* **16**, 229 (2020).
- [45] A. Singh, C. Ness, A. K. Sharma, J. J. de Pablo, and H. M. Jaeger, *arXiv preprint arXiv:2311.05696* (2023).
- [46] R. C. Ball and J. R. Melrose, *Adv. Colloid Interface Sci.* **59**, 19 (1995).
- [47] P. A. Cundall and O. D. L. Strack, *Geotechnique* **29**, 47 (1979).
- [48] S. Luding, *Gran. Matt.* **10**, 235 (2008).
- [49] A. Singh, V. Magnanimo, K. Saitoh, and S. Luding, *New J. Phys* **17**, 043028 (2015).
- [50] L. E. Silbert, *Soft Matter* **6**, 2918 (2010).
- [51] T.-Y. Lin, P. Goyal, R. Girshick, K. He, and P. Dollár, in *Proceedings of the IEEE international conference on computer vision* (2017) pp. 2980–2988.
- [52] B. J. Erickson and F. Kitamura, “Magician’s corner: 9. performance metrics for machine learning models,” (2021).

**SUPPLEMENTARY INFORMATION TO:
APPLICATION OF GRAPH NEURAL NETWORK IN PREDICTION OF FORCE CHAIN NETWORKS
IN SUSPENSIONS**

In this document we provide details about (i) simulation methodology; (ii) training method; (iii) training parameters & process; and (iv) further calculations complementing the ones presented in the main text.

LF-DEM SIMULATION METHODOLOGY

Simulation Method

For training the GNN, we simulate an assembly of inertialess frictional spherical solid, immersed in a Newtonian fluid of viscosity η_0 under various imposed shear stresses (σ_{xy}). Simulating at fixed stress means that the suspension flows with time-dependent shear rate $\dot{\gamma}(t)$. We simulated $N = 400$ to 5000 non-Brownian bidisperse particles with Lees-Edwards periodic boundary condition in a unit cell with radii of a and Δa , with Δ in the range of $\{1.4, 6\}$ for various values of volumetric mixing ratio $\alpha = [0.1, 0.9]$. The equation of motion is a balance of the interactions between particles subject to short-range hydrodynamic forces (F_H), Repulsive forces (F_R), and frictional contact forces (F_C) [36].

$$0 = \mathbf{F}_H(\mathbf{X}, \mathbf{U}) + \mathbf{F}_C(\mathbf{X}), \quad (1)$$

with \mathbf{X} and \mathbf{U} referring to the particle position and velocities, respectively. We regularize the lubrication force, allowing the particles to make contact as the overlap ($\delta^{(i,j)} = a_i + a_j - |\mathbf{r}_i - \mathbf{r}_j|$) becomes positive [11, 46]. Here, a_i and a_j refer to particle radii, and \mathbf{r}_i and \mathbf{r}_j represent the position vectors of the center of particles i and j , respectively. The contact force is modeled using traditional Cundall & Strack [47] and following the algorithm described by Luding[48]. We employ linear springs in normal k_n and tangential k_t directions to model contacts between particles, which are tuned such that the maximum scaled particle overlap does not exceed 3% and the rigid particle approximation is satisfied [49]. In our simulation, we do not use dashpot; instead, the hydrodynamic resistance provides energy dissipation [32]. The tangential component of contact force satisfies Coulomb's friction law $|\mathbf{F}_C^t| \leq \mu |\mathbf{F}_C^n|$ with $\mu = 0.5$ being the static friction coefficient. We use two particle sizes with size ratio $\Delta = R_L/R_S$ mixed in a volumetric mixing ratio $\alpha = N_S a_S^3 / (N_S a_S^3 + N_L a_L^3)$ with N_L and N_S denoting the numbers of large and small particles with respective radii being a_L and a_S . We use the so-called Critical Load Model (CLM) to introduce rate dependence, where frictional force is activated above a threshold normal force F_0 , which provides a characteristic stress scale $\sigma_0 = F_0/a^2$ (in the traditional approach a is defined in the monodisperse limit, and we assume F_0 to be insensitive of particle size). Further details about the simulation scheme are available in Refs. [10, 11, 32, 34, 36, 45].

Figure SS1 depicts the rheological results obtained from simulations. As shown, that increase in stress level σ/σ_0 leads to an increase in viscosity η_r (Fig. SS1b), which is associated with stress-activated transition from frictionless to frictional contacts (Fig. SS1a). As the frictional contacts (solid symbols) increase with stress, the frictionless coordination number (open symbols) decreases above the onset stress of $\sigma/\sigma_0 = 1$. Both, the bulk response, i.e., viscosity η_r and frictional coordination number Z_μ mirror each other. Fig. SS1b displays rheological response, where continuous shear thickening is observed for $\phi = 0.76$ & 0.78, while suspension undergoes discontinuous shear thickening (DST) for $\phi = 0.8$, note the S-shaped $\eta_r(\dot{\gamma})$ flowcurve for $\phi = 0.8$ (Fig. SS1c) Note that at $\phi = 0.8$, the suspension is very close to being shear-jammed (SJ) with frictional coordination number being very close to the isostatic condition $Z_{\text{iso}} = 3$ for frictional particles [50].

Figure S2 shows a typical force network obtained from the simulations at a packing fraction of $\phi = 0.80$ with increasing stress σ/σ_0 from left to right. Line segments connect the centers of two contacting particles and are color-coded with the type of force they experience; we show frictional (black line) and frictionless contacts (blue line). Clearly, as the shear stress increases, we go from a mixed state of frictionless (blue line) and frictional (black lines) contacts at $\sigma/\sigma_0 = 5$ to a fully frictional state (only black lines) at $\sigma/\sigma_0 = 100$. This visual observation is consistent with Fig. S1.

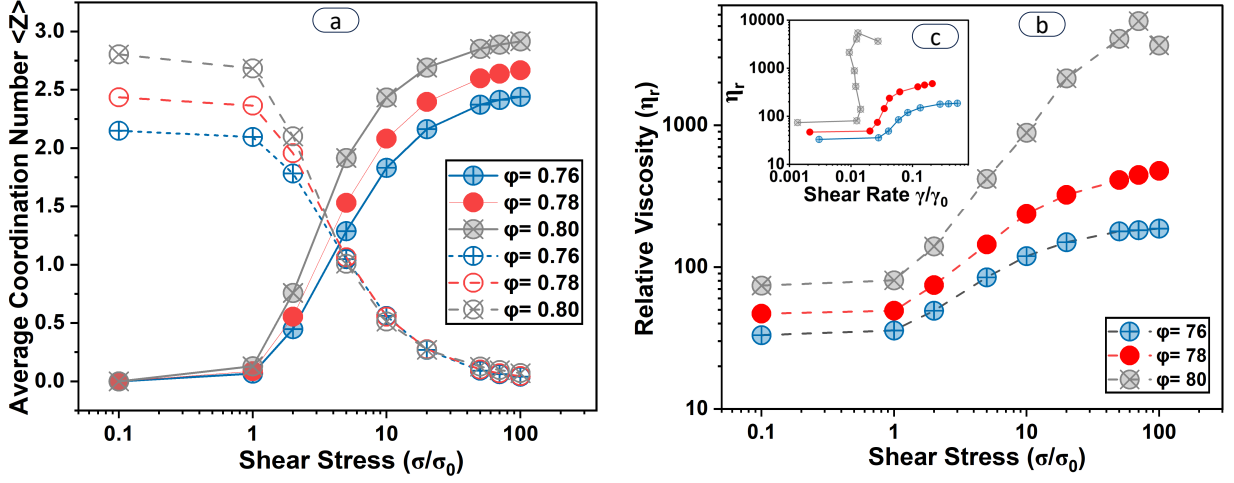


FIG. S1. Evolution of microscale structures and the rheological response of the material. (a) Mean number of particle-particle contacts $\langle Z \rangle$; with solid symbols representing frictional contacts (friction is activated), open symbols representing frictionless contacts (friction is not activated). (b) shear viscosity η_r plotted as a function of shear stress σ/σ_0 . (c) shear viscosity η_r plotted as a function of shear rate $\dot{\gamma}/\dot{\gamma}_0$. Different symbols represent different packing fractions.

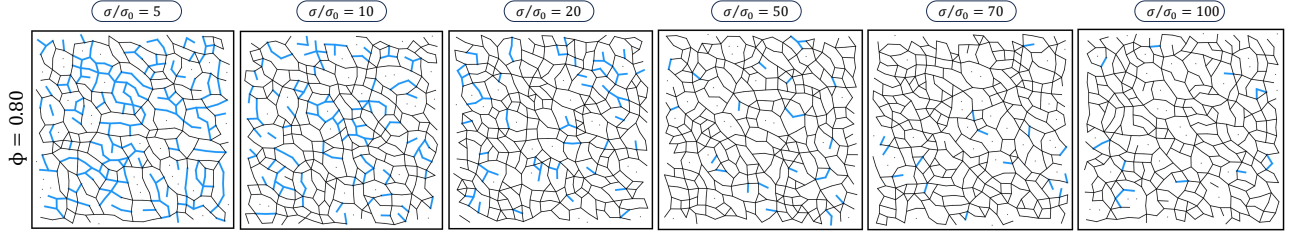


FIG. S2. Development of frictional contacts with increasing shear stress. Blue lines represent frictionless contacts (friction is not activated), and black lines represent frictional contact (friction is activated).

Training Method

The first step in predicting the Force chain Network (FCN) within a suspension using Graph Neural Networks (GNN) involves converting the configuration into a graph. In this representation, each particle is denoted as a node, and an edge connects two nodes if the respective particles are in frictional contact. In the graph, each edge is associated with edge features (e_0) which include the distance between particles ($|r_{ij}|$), x and y components of \mathbf{r}_{ij} , and Sine and Cosine of angle \mathbf{r}_{ij} makes with the flow direction. Each node contains one hot-coded feature n_0 of its related particle radius. Then, we subject the node and edge features to a linear transformation that incorporates weight matrices ($W(n)$ and $W(e)$), bias vectors (b_n and b_e), and a hidden dimension (d_h) which controls the capacity or expressive power over model [26]. This transformation enables our model to map the input features into a higher-dimensional space, empowering the model to learn and represent more intricate patterns and relationships within the dataset.

$$n'_0 = W^{(n)}n_0 + b_n \quad (2)$$

$$e'_0 = W^{(e)}e_0 + b_e \quad (3)$$

Next, edge and node features are passed through N_l layers of a residual graph convolutional network (ResGCN) that adds a layer's original input to its output, creating a skip connection. This mitigates information loss during the learning process and enables more effective training of deeper graph neural networks [39, 40].

$$h_v^l = h_v^{l-1} + \sum_{u \in N(v)} S(W_f^l(z_{v,u}^{l-1}) + b_f^l) \odot R(W_s^l(z_{v,u}^{l-1}) + b_s^l) \quad (4)$$

Here, $h_v^{(l)}$ is the updated node feature or hidden state for node v at layer l , $\mathcal{N}(v)$ denotes the neighborhood of node v , i.e., the set of nodes connected to v . f is a function that takes as input the features of neighboring nodes, i.e., $h_v^{(l-1)}$ and $h_u^{(l-1)}$ and their edge features e_{uv} , concatenating the features and applying non-linear aggregation function, $\sum_{u \in \mathcal{N}(v)}$ is the summation over all neighboring nodes u of node v and $h_v^{(l-1)}$ is the original node feature which will be added to the output of GCN. W_f^l and W_s^l are the trainable weight matrices acting on the node and edge features, and b_f^l and b_s^l are the bias vectors. $z_{u,v}^{l-1}$ is the concatenating vector of the nodes v and u along with their edge feature $e_{v,u}$ in the previous layer. \odot represents element-wise multiplication. S and g are aggregation function $S = e^{x_i} / \sum_j e^{x_j}$ and activation function, $\text{ReLU}(x) = \max(0, x)$, respectively. We used **Pytorch Geometric DeepGCN** package to implement our ML.

During training, the model’s parameters are adjusted iteratively to align the predicted outputs more closely with the actual targets through the loss function. Traditional cross-entropy (CE), also known as categorical cross-entropy or log loss, is a widely used loss function in machine learning, particularly in classification tasks. In the **Binary CE (BCE)** with logits, there are only two possible classes (commonly denoted as 0 and 1), the goal is to predict the probability that an instance belongs to class 1 (the positive class, particles are in contact). In contrast to standard BCE, it merges a Sigmoid function and the conventional BCE into a single class, providing numerical stability compared to using a separate Sigmoid followed by a conventional BCE.

$$\text{BCE} = -w_n [p_i \log \sigma(q_i) + (1 - p_i) \log(1 - q_i)] \quad (5)$$

Here, w_n is a manual rescaling weight, p_i denotes the true probability, and q_i is the predicted probability of the instance belonging to class 1 according to the model. This relationship penalizes the model when it predicts a probability close to 0 for the case the actual data belongs to class 1 and vice versa. For instance, in the case of a prediction belonging to class 1 ($p_i = 1$), the loss term is $-\log(q_i)$, while belonging to class 0 ($p_i = 0$), the loss term is $-\log(1 - q_i)$. The major limitation of CE is that it treats all classes equally, which can be problematic in the case of an imbalanced data set and thus can make the model biased toward the majority class.

To improve model performance and tackle imbalanced datasets, we experimented with various loss functions such as weighted cross entropy, a modified version of CE where we can manually insert a rescaling weight value, and focal loss [51], allowing us to adjust the contribution of each class by manipulating factors. Although BCE worked well for most predictions, focal loss and weighted cross entropy led to 1-3% better accuracies in scenarios where the model was trained with $\sigma/\sigma_0 = 10$ and $\phi = 0.76$.

Hyperparameters were determined by analyzing loss values for both the training and testing configurations. Ultimately, we selected hyperparameters, d_h set to 64, N_l of 2, and a learning rate (λ) of 0.005. This systematic approach ensures the optimization of the model’s performance based on empirical evidence from the training and testing phases.

Training Parameters & Process

Fig. SS3 illustrates the loss function and accuracy trends across epochs during the model training. Our training dataset comprised 320 configurations (80% of our overall dataset), while a set of 80 configurations (20% of the dataset) was reserved for testing the model’s performance. We stop the training process when the loss value doesn’t improve after 15 epochs by saving the last iteration parameters at which the loss is minimum. Subsequently, we employed 400 previously unseen configurations for validation purposes well beyond the initially seen training conditions. These predictions derived the reported average prediction accuracy of the FCN.

Conventional performance metrics such as accuracy can be deceptive in an imbalanced dataset where one class is much more dominant than the other. A model can reach high accuracy by considering the majority class for all instances, disregarding the minority class completely. Several metrics are used to better illustrate a model’s performance in an imbalanced dataset [52]. In addition to average accuracy, we measured average precision measure, recall, F1 score, AUC, and specificity.

Precision assesses the ratio of correctly predicted positive instances to the total number of positive predictions made by the model. Recall, referred to as sensitivity, evaluates the fraction of actual positive cases in the dataset that are correctly identified as positive by the model. metrics focus on the model’s performance in the positive class. The F1 score considers precision and recall, making it a more balanced measure for imbalanced datasets. It ensures that the model performs well for both the majority and minority classes. AUC evaluates the model’s ability to differentiate between positive and negative classes over a range of threshold settings. It is insensitive to class distribution and provides an aggregate measure of model performance. Specificity quantifies the model’s effectiveness in accurately detecting negative instances from the total of actual negative instances. [52]. It complements sensitivity and is

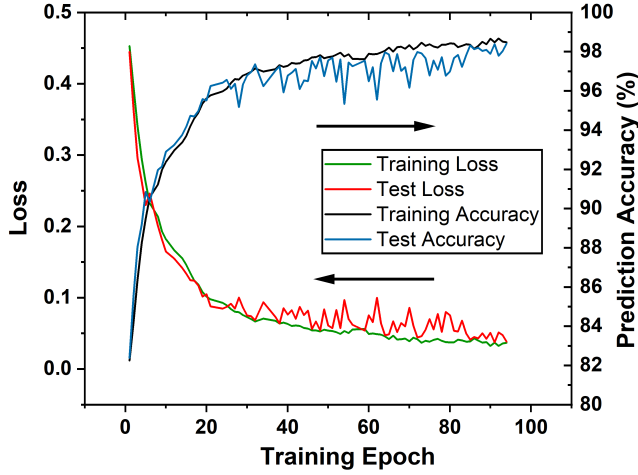


FIG. S3. Prediction Accuracy and Loss function (Binary cross entropy) for training the model at $\phi = 0.80$ and $\sigma/\sigma_0 = 10$ with 320 graphs and a set of 80 graphs for testing using early stop training.

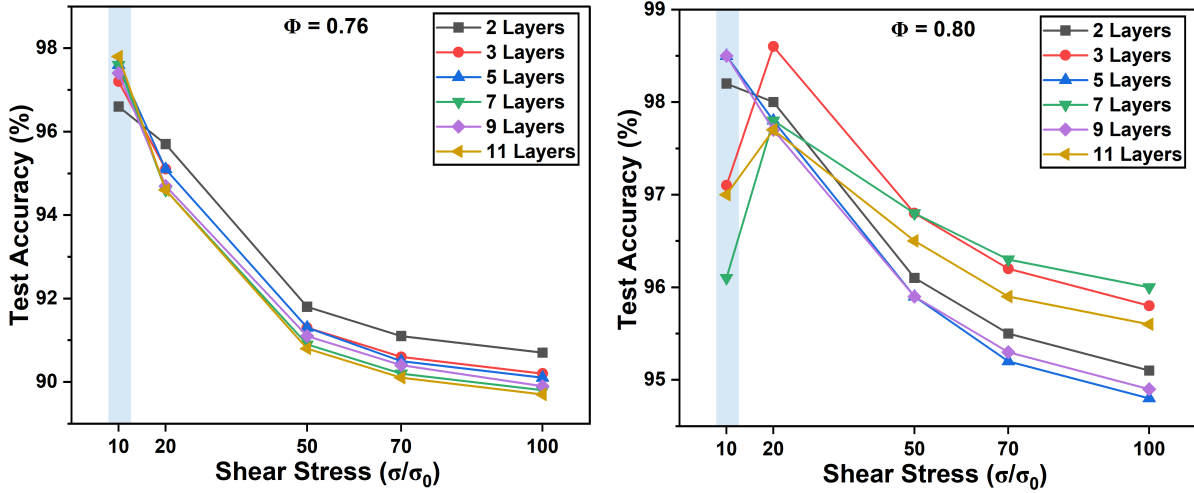


FIG. S4. Test accuracy as a function of σ/σ_0 for two values of $\phi = 0.76$ and 0.80 while all have been trained at $\sigma/\sigma_0 = 10$ with different number of layers of DeepGCN.

especially relevant in imbalanced datasets with the predominant negative class. Since the F1 score and AUC are relevant metrics for imbalanced datasets, their high values alongside high accuracy reinforce the model's ability to handle the imbalance.

According to the results obtained for our model trained at packing fractions of ϕ of 0.76 and 0.80 and stress $\sigma/\sigma_0 = 10$ (Table SS1), all the metrics, including F1 score and AUC, are high and close to the value of average accuracy indicating the robustness of our model to capture both classes. For example, the prediction results for $\phi = 0.8$ and $\sigma/\sigma_0 = 50$ show a high precision value, meaning 97.3% of the time the model predicts something as positive, it's positive; a high Recall value indicating the model catches 96.1% of the actual positive cases; an exceptionally high specificity, meaning the model rarely identifies negative cases as positive (only 0.2% misclassification); a very good F1 score (96.4%), indicating a high balance between precision and recall; and a high AUC value (97.8%), meaning the model can effectively distinguish between positive and negative cases.

Obtaining optimum number of layers: When the model is trained with an increased number of layers, the process of message-passing delves deeper into the network, extracting information from nodes that extend beyond its immediate neighbors. This augmentation proves particularly beneficial in scenarios where obtaining extensive information is crucial for enhancing predictive accuracy, especially when considering the long-range interactions among particles, which can significantly influence the force chain network and overall rheological response. Fig. SS4 illustrates the

TABLE S1. Comparison between different metrics to evaluate the performance of machine learning at two ϕ s of 0.76 and 0.80 and σ/σ_0 of 10 to 100

σ/σ_0	ϕ	Average Accuracy	Weighted F1-Score	Precision	Recall	Specificity	AUC-ROC
10	0.76	0.966	0.965	0.967	0.966	0.862	0.931
	0.80	0.982	0.982	0.983	0.982	0.904	0.952
20	0.76	0.957	0.959	0.966	0.957	0.992	0.971
	0.80	0.98	0.981	0.983	0.98	0.99	0.984
50	0.76	0.918	0.928	0.954	0.918	0.999	0.954
	0.80	0.961	0.964	0.973	0.961	0.998	0.978
70	0.76	0.911	0.923	0.954	0.911	0.999	0.95
	0.80	0.955	0.96	0.971	0.955	0.999	0.975
100	0.76	0.907	0.92	0.955	0.907	1	0.949
	0.80	0.951	0.956	0.97	0.951	1	0.973

model’s efficacy under initial conditions with values of $\phi = 0.76$ and 0.80 as a function of σ/σ_0 with different numbers of deepGCN layers, showcasing the performance across varying layer depths. Notably, even with a shallow model architecture featuring just two layers, the prediction is highly accurate and emphasizes the robustness of the model’s capabilities. Scientifically, this highlights the model’s adeptness in capturing intricate relationships and dependencies within the data. Regarding the lower accuracies for $\phi = 0.76$, as the number of deepGCN layers are varied from 2 to 11 without a significant impact on the accuracy. This suggests that factors beyond the number of layers might be influencing performance, such as adjustments to other training parameters. Beyond a certain depth (2 layers) the performance of the GNN deteriorates regardless of the parameter ϕ it’s trained with. This could indicate an issue with overfitting or vanishing gradients as the network becomes deeper. This suggests that as the GNN processes messages over layers, the node representations become increasingly similar to their neighborhood information. This could lead to a loss of discriminative power, causing the model’s generalization performance to worsen.

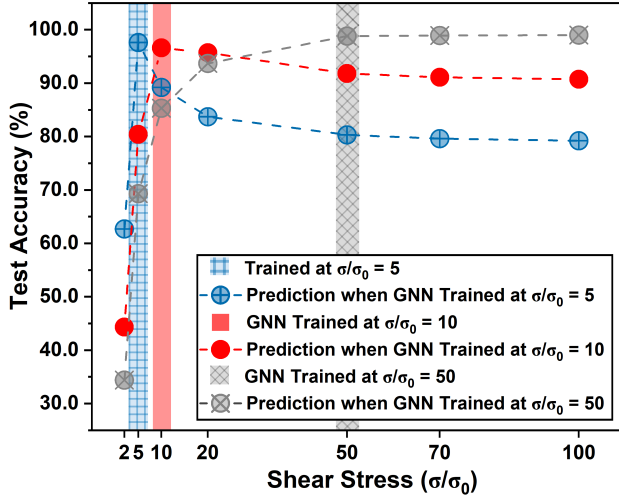


FIG. S5. Test accuracy as a function of σ/σ_0 while the models have been trained at different σ/σ_0 of 5, 10, and 50.

Training at different stress levels: In the main text, we presented results when the model is trained for a stress $\sigma/\sigma_0 = 10$ (Fig. 2 on the main text). The natural question arises about the validity of results as the system is trained at different stress levels. Figure SS5 illustrates test accuracy results when the model is trained at different values of σ/σ_0 . While the predictions for the model trained at a $\sigma/\sigma_0 = 5$ are unsatisfactory, the predictions improve significantly when the model is trained at $\sigma/\sigma_0 = 10$ and 50. It is important to note that this is an extrapolation task, which is inherently more challenging for the model, especially given that the rheological properties of suspensions vary with σ/σ_0 .

To explore the physical rationale behind this, Fig. SS6 illustrates the evolution of contact chains and structure factors with increasing shear stress. As pointed out already in Figs. S S1 and S S2, the number (of fraction) of frictional contacts begin to saturate (frictionless contacts diminishing) in the limit of $\sigma/\sigma_0 \geq 10$, which implies the physics is fully dominated by frictional contacts in that regime. Although the evolution trend appears similar, the number of contacts (denser force chain network) is observed for higher packing fraction $\phi = 0.8$. This discrepancy is evident, particularly at low shear stress levels (e.g., 10), after which both configurations follow the same trend reaching saturation.

Predictions for different volumetric mixing ratio α : Fig. SS7 illustrates the prediction of FCN for systems with size ratio $\Delta = 1.4$, and various values of volumetric mixing ratio of small particles $\alpha = [0.1, 0.3, 0.5, 0.7, 0.9]$ when it has been trained only at $\alpha = 0.5$. We observe a good accuracy based on two observations (i) very minimal red colored particles (red particles show instances where the contact is not correctly predicted), and (ii) low absolute error in predicting the structure factor. In the main text, we have demonstrated that the model can accurately capture the FCN when trained at $\alpha = 0.1$ or $\alpha = 0.9$.

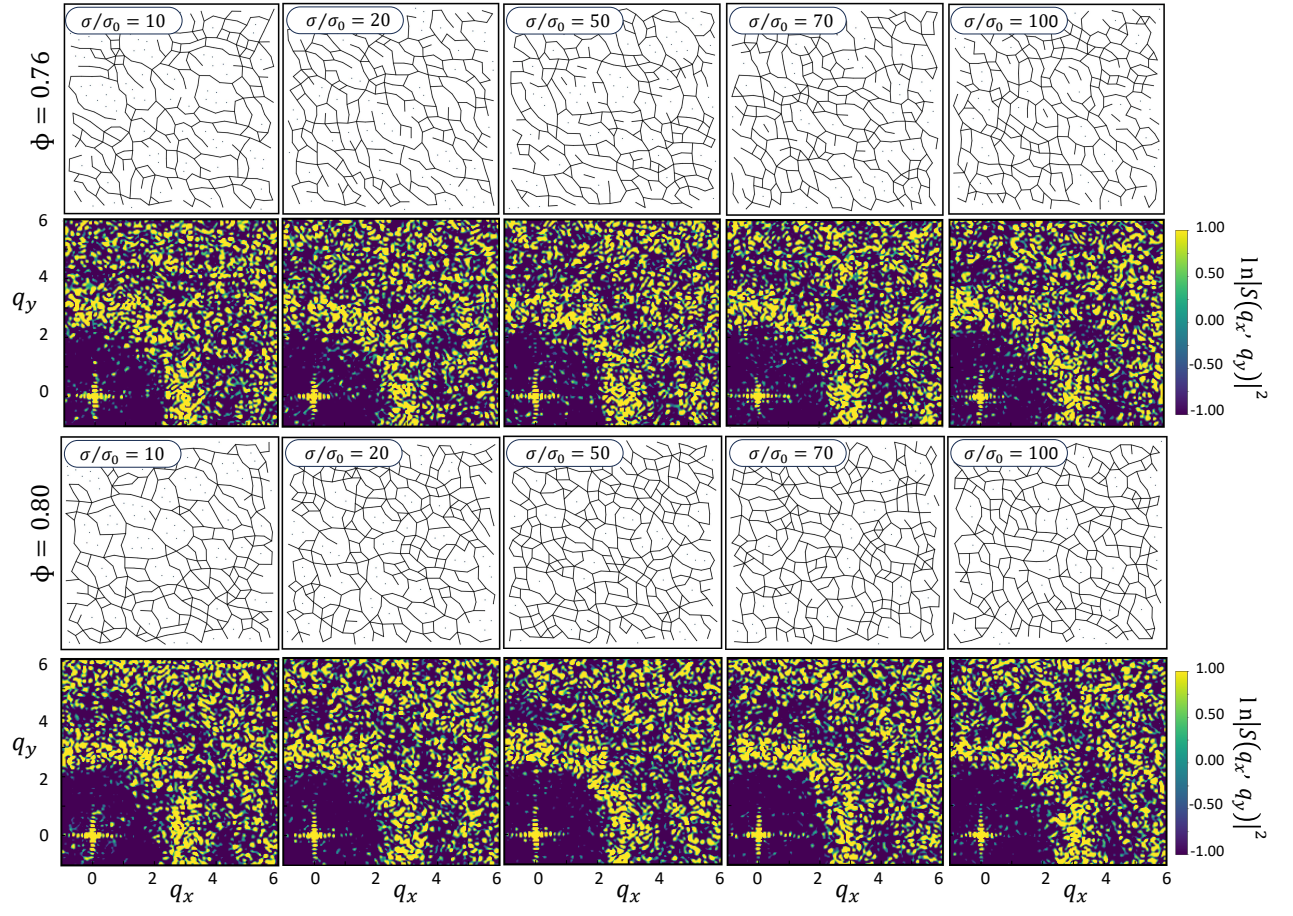


FIG. S6. Prediction of FCN with its corresponding structure factor at two different values of ϕ when the models are only trained at the shear stress of 10. Top row indicating the prediction at various stresses at $\phi = 0.76$, the bottom row is the same but for $\phi = 0.80$.

Predictions for different size ratios Δ : Fig. SS8 and SS9 exhibit the prediction of FCN for systems consisting of $N = 400$ and 2000 particles at various values of particle size ratios (Δ) from 2 to 6 (for a constant $\alpha = 0.5$) when the model is only trained at $\Delta = 1.4$ and configuration with $N = 400$ particles.

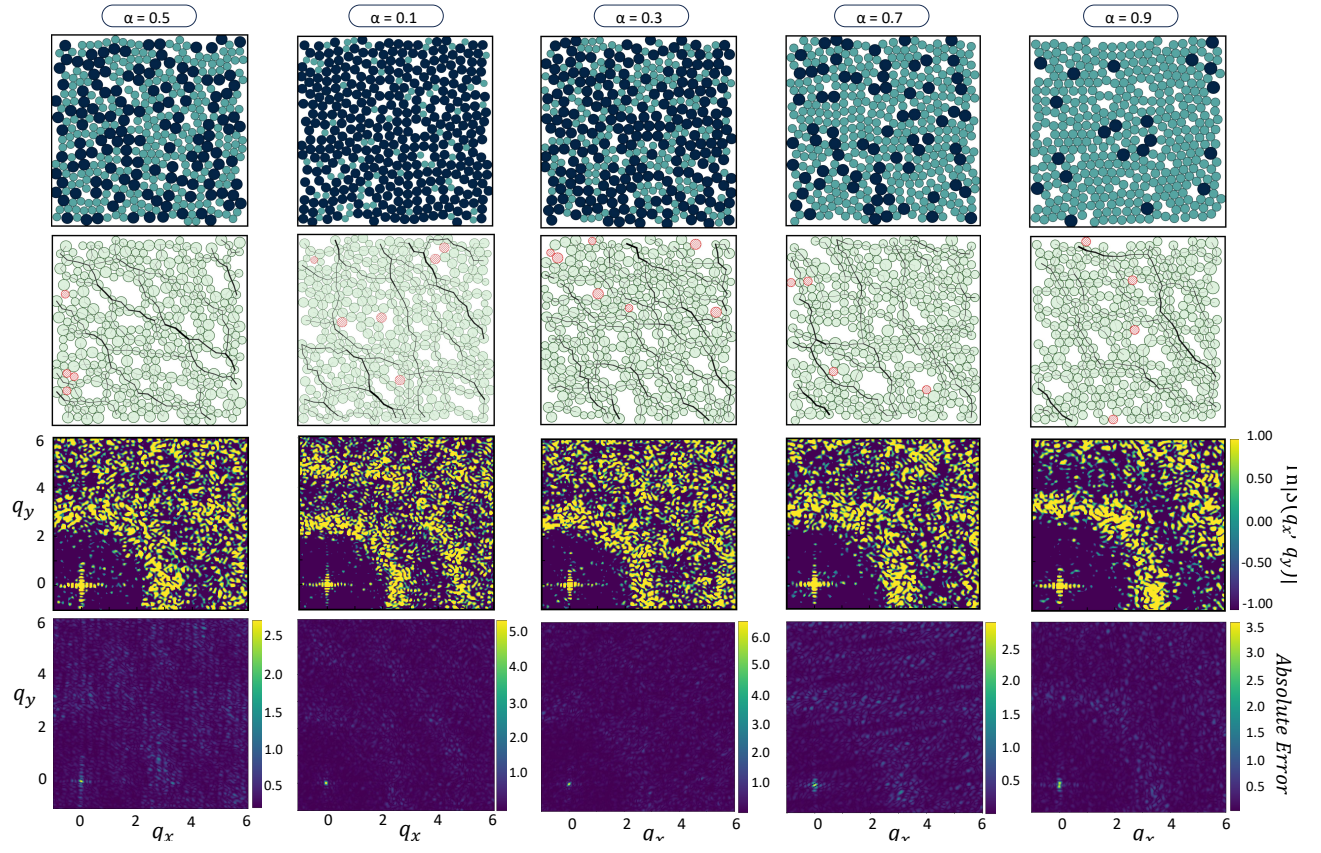


FIG. S7. Prediction of FCN for systems with various packing fraction of volumetric mixing ratio (α) from 0.1 to 0.9 when the model has been trained only at $\alpha = 0.5$.

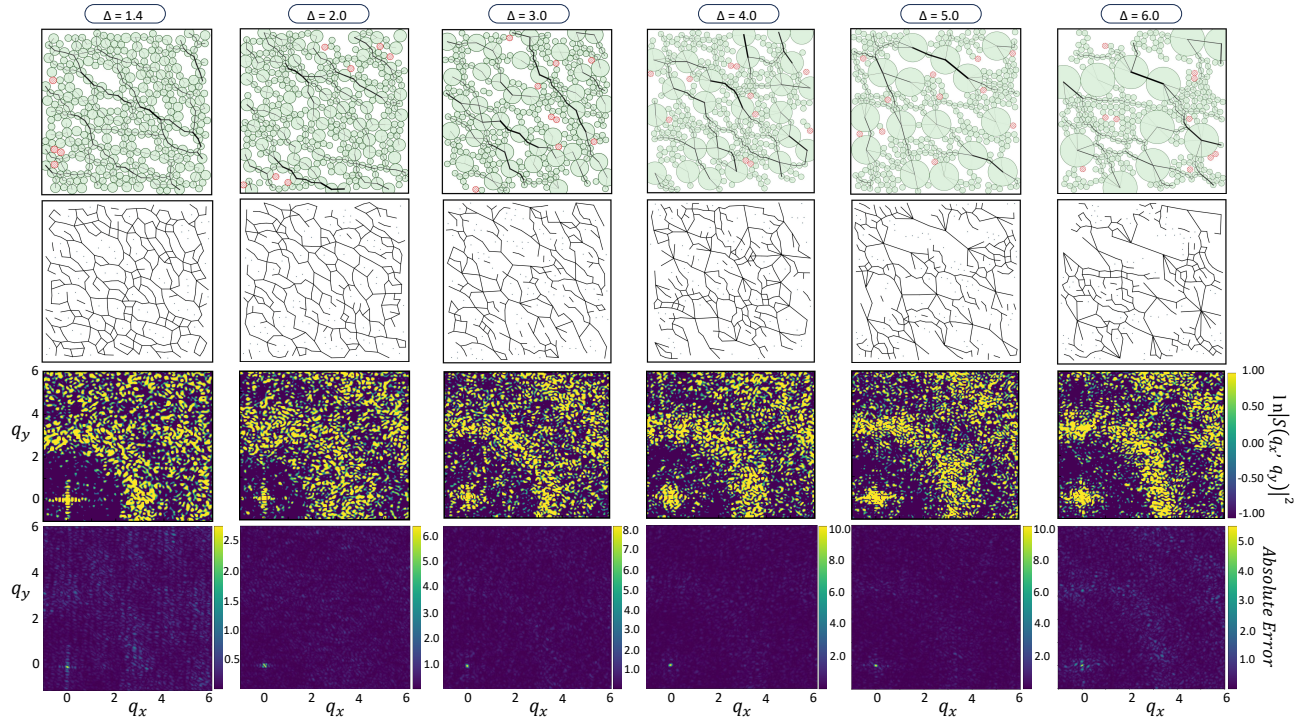


FIG. S8. Prediction of FCN for systems consisting of $N = 400$ particles at various particle size ratios (Δ) from 2 to 6 when the model is only trained at $\Delta = 1.4$

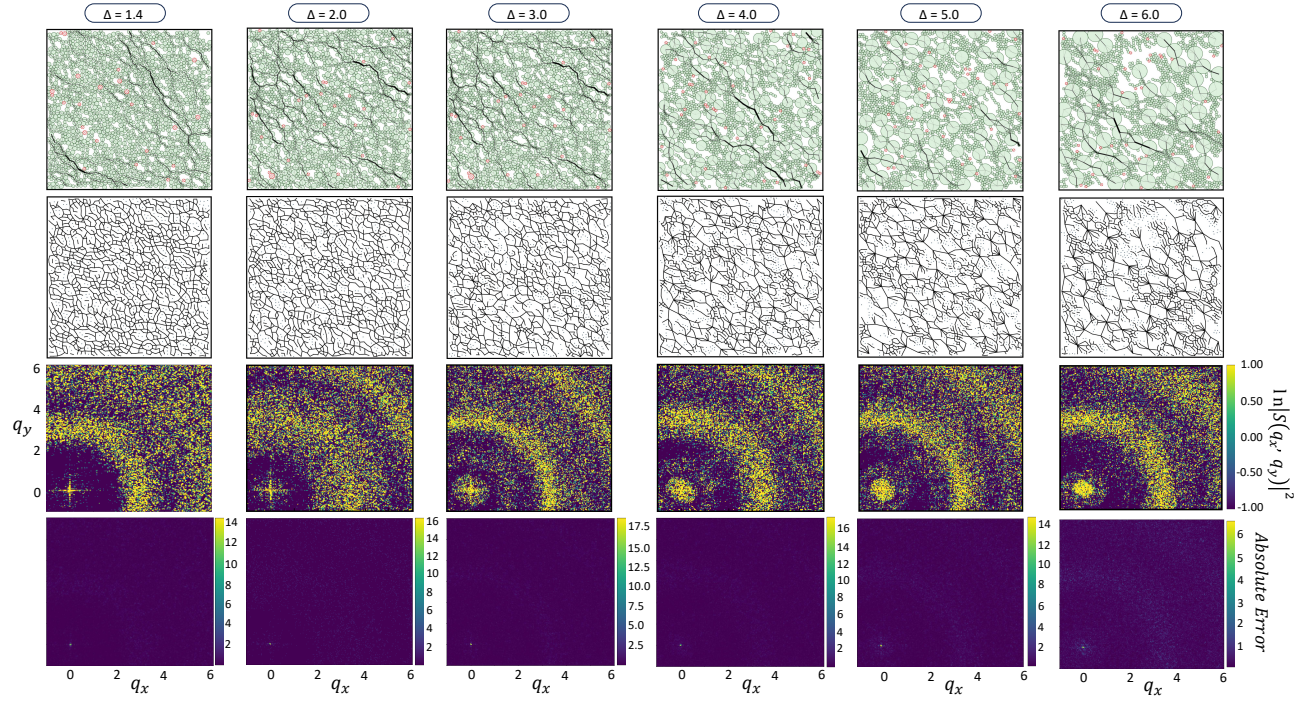


FIG. S9. Prediction of FCN for systems consisting of $N = 2000$ particles at various particle size ratios (Δ) from 2 to 6 when the model is only trained at a configuration with $N = 400$ particles and $\Delta = 1.4$